Fachtagung "Lasermethoden in der Strömungsmesstechnik"
4.–6. September 2012, Rostock

Erosion of a Strong Density Stratification by a Vertical Air Jet

Erosion einer Dichtestratifizierung durch einen vertikalen Luft Jet

R. Kapulla*, G. Mignot*, D. Paladino*
*Labor für Thermohydraulik (LTH), Paul Scherrer Institut, 5232 Villigen, Schweiz

Abstract

Computational Fluid Dynamics (CFD) codes are increasingly used for safety analysis to simulate transient containment conditions after various severe accident scenarios in Nuclear Power Plants (NPP). Consequently, the reliability of such codes must be benchmarked against experimental data obtained in large scale facilities. Inspired, but not restricted to these accident scenarios, a series of fundamental mixing experiments were performed in the large scale PANDA test section built at the Paul Scherrer Institute in Switzerland, highlighting the interaction of a vertical air jet emerging from a tube below a helium-rich air layer. The isothermal experiments address the (i) the mechanisms of the gas transport and the (ii) entrainment of the helium stratification located just beneath the vessel dome. The experiments were conducted under conditions characterized by an initially non-buoyant jet which becomes negatively buoyant and rapidly decelerates when it reaches the helium stratification. For comparison purposes, additional experiments were performed for a pure, non-buoyant air jet emerging into the vessel in the absence of the helium stratification but, having the same exit velocity as the stratified case. For the stratified experiment it is shown that the axial velocity $\overline{v}$ decays much faster already below the jet impingement zone compared with a corresponding free air jet while the turbulent kinetic energy k remains on the same level as for the free jet until it levels off once the stratification is reached.

1 Introduction

A jet of fluid with density ρ_j which is directed into a volume of fluid of density ρ_a with $\rho_j \neq \rho_a$ or a jet (ρ_j) impinging onto a stable density stratification (ρ_a) is encountered in industry and at work. The sewage disposal through a pipe into a river or the sea is industrially widespread used to mix the wastewater with fresh water. For example, after the cooling of a power plant. Using an air conditioner for the heating or cooling of a room, a jet of different temperature and therefore different density may be forced into the room through a ceiling vent. Buoyant jets resulting from temperature and / or salinity differences can occur in the ocean and the atmosphere. An overview of the different phenomena and the physics in buoyant turbulent jets can be found in [6, 1].

A jet with the density ρ_j is called *positively buoyant* when the jet fluid is injected vertically upwards into an ambient fluid with a higher density ρ_a. The buoyancy force and the momentum have the same direction and the buoyancy force adds to the momentum such that the velocity decay, common for non-buoyant jets is partly compensated and for strong buoyancy forces the jet might even accelerate. When the buoyancy and the momentum forces have opposite directions the jet is called *negatively buoyant*, i.e. the negative buoyancy decelerates the jet much faster compared with a non-buoyant jet.

The experiments presented in the paper describe the interaction of a vertical, upward projecting air jet emerging from a tube below a helium-rich air layer. The isothermal experiments address the (i) the mechanisms of the gas transport and the (ii) entrainment of the helium stratification located just beneath

the vessel dome. The experiments were conducted under conditions characterized by a jet which is initially non-buoyant and becomes negatively buoyant and decelerates when it reaches the helium stratification. Results depicting the mixing, transport and transient helium stratification erosion are presented in terms of 2D PIV measurements which were used to measure the flow velocities at different locations and in particular at the interface between the helium layer and the upward flowing jet. Additional gas concentration profiles measured with a mass spectrometer are used to illustrate the erosion process of the density stratification. Initially, the vertical jet discharges into a neutral environment, i.e. $\rho_j = \rho_a$ and therefore has physical characteristics similar to a classical non-buoyant jet. After a certain distance, the ambient density continuously decreases such that the non-buoyant jet becomes increasingly negatively buoyant when penetrating the helium rich layer and the axial velocity decays very rapidly. Fluid accumulates in this mixing zone and a part of the fluid is flowing back in a small annulus around the upward flow. By this transient mechanism, the helium layer is continuously eroded and helium is transported into lower parts of the test section such that the jet becomes increasingly negatively buoyant right from the beginning.

In the next section we give a brief introduction of the experimental facility, the instrumentation and the experimental parameters. For comparison purposes, we start presenting turbulence characteristics for a pure air jet emerging into the vessel in the absence of the helium stratification but, having the same exit velocity as the stratified case. These results are compared with the literature. In the second part we discuss the details of the erosion process in the presence of a helium rich stratification. Although a complete experimental series was perform with varying initial jet velocities and different stratification strengths, we will focus the presentation on one unstratified and one stratified jet experiment.

2 Experiments

This section provides a brief overview of the facility, the instrumentation used for the experiments and the experimental parameters. The experiments were performed in a vessel having an inner diameter of 4 m and a height of 8 m, Figure 1. The air for the jet is injected through a tube at the axis of symmetry of the vessel. The injection tube has a 90 ° bend close to the bottom of the vessel. Since the straight tube past the bend has a length of $> 15d_t$ it is expected that possible disturbances introduced by the bend are removed by the turbulence due to the high tube Reynolds number $\mathrm{Re}_0 = 14'000$, Table 1. Consequently,

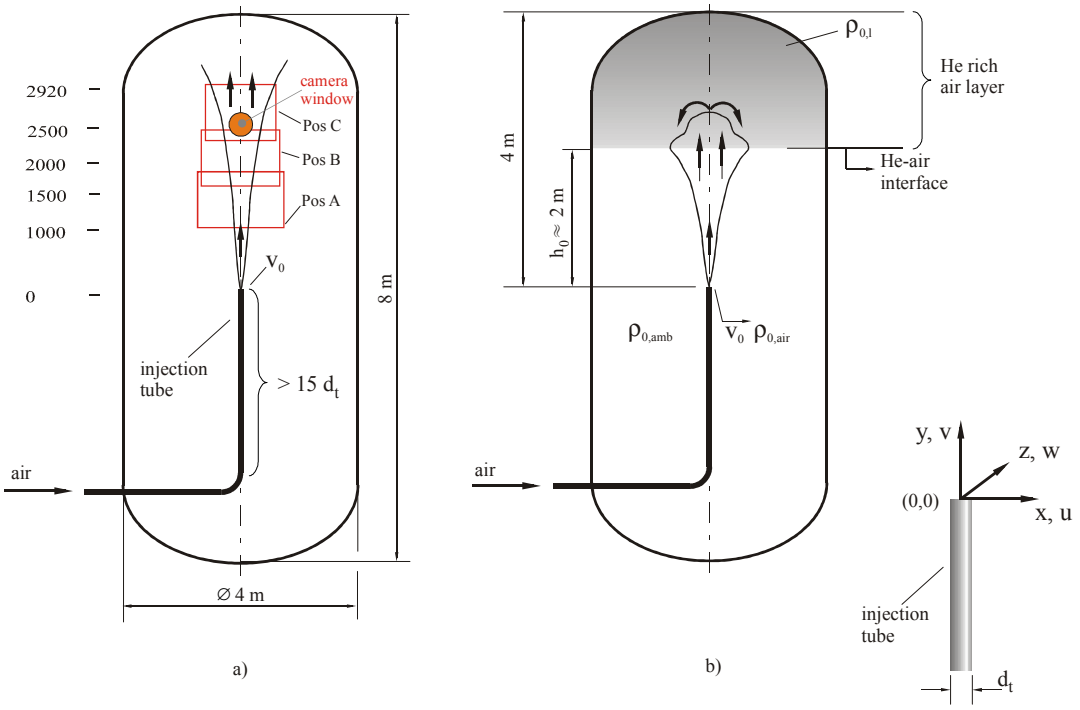

Figure 1: *Schematic of the experimental setup for the pure air jet a) and the air jet with helium rich air layer in the vessel dome b).*

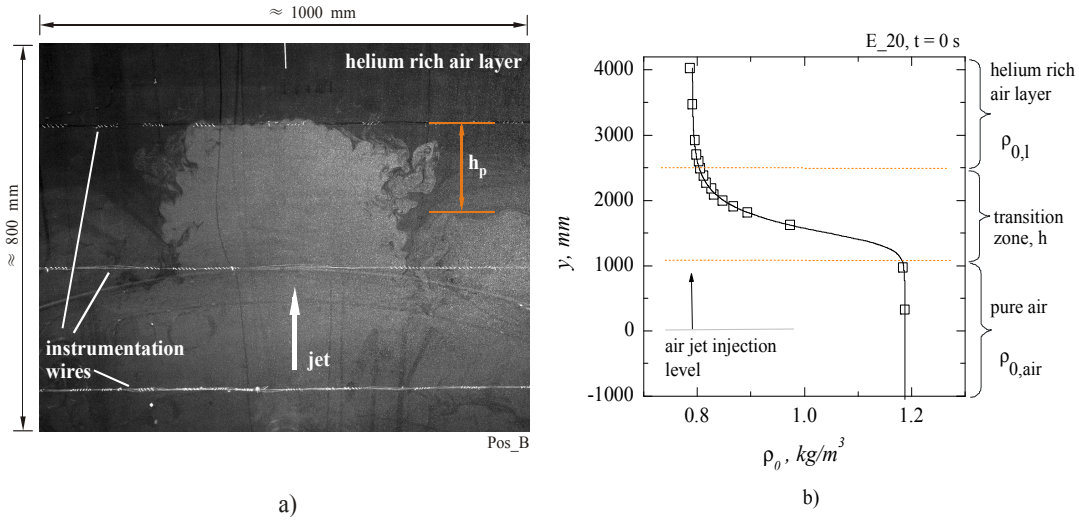

Figure 2: *Example PIV image recorded at position B showing the seeded jet from below, the non seeded helium rich air layer at the top and the horizontal instrumentation wires a). Initial density profile recorded in the symmetry axis of the test section b).*

the velocity profile at the tube exit are expected to show top hat characteristics with boundary layers typical for turbulent pipe flows. In contrast to some past jet experiments where a smooth contraction nozzle at the tube exit was used to pronounce the top hat velocity profile by compressing the boundary layers, we used an injection tube with a constant inner diameter of $d_t = 0.075\ m$. For a comparison between the two types of initial velocity profiles for straight and contraction nozzles at the tube exit see Fig. 1 in [8] . The pressure was kept constant at 1 bar absolut by venting the vessel through a tube located at the bottom of the vessel.

The tube exit is located $4\ m$ above the bottom of the test section to avoid any wall effects in the vicinity of the tube exit. The coordinate system origin to describe the experiments is located at the injection tube exit and the light sheet for the PIV recordings coincides with the $x - y$ plane, Figure 1. The PIV camera was mounted in front of an upper vessel window on a translation stage consisting of two goniometer and a rotation table. By vertically inclining the camera it was either possible to record three different field-of-views (FOV) for the steady state jet experiments or to follow successively the erosion front for the jet-layer experiments. The three FOV's are depicted as Pos_A, Pos_B and Pos_C in Figure 1 a). An example for a PIV image recorded at position B is shown in Figure 2 a). The image gives an impression of the jet-layer interaction zone. The seeded jet entering from below impinges onto the non seeded helium rich layer and penetrates the stratification. Olive oil, dispersed into small droplets by a spray nozzle, was used as seeding particles for the PIV technique. The oil particles were injected into the air injection tube that was directed into the vessel through the injection line. The PIV system provides 2D velocity fields with a typical acquisition rate of $5\ Hz$. For the calculation of statistical quantities 2048 image pairs were averaged. The PIV system consisted of a Quantel Twins B double pulse laser with a maximum output energy of $380\ mJ$ and a double frame CCD camera type Imager Pro X which is identical to the PCO.1600 camera, with a resolution of 1600x1200 pixel. The base analysis was performed with DaVis 7.2 and the extended analysis with in house written MATLAB routines. For the base analysis consisting in the calculation of the instantaneous velocity vector maps, the image background calculated as the mean of all the raw PIV images was subtracted and we applied a multi pass analysis with decreasing window sizes ($128 \rightarrow 64 \rightarrow 32$) where for each window size the velocity was calculated with two passes. The velocity fields for interrogation window sizes of 128x128 and 64x64 was calculated with $0\ \%$ overlap while we used $50\ \%$ overlap for the final size of 32x32, i.e. an effective spatial resolution of 16x16. For the de-warping of the images, i.e. the translation of the raw pixel coordinates to physical units and the removal of perspective distortions arising from the inclination of the camera with respect to the calibration target, we used the DaVis built-in so called 'high accuracy mode' for the final pass of the velocity calculation which consists in a Whittaker reconstruction of the images. Although much more time consuming this was necessary to result in reliable velocity statistics, since the standard reconstruction resulted for some (but not all) rms velocity fields in un-physical moire patterns.

After calibration of the images we had a resolution of 0.625x$0.625\ mm^2/pixel$ which corresponds to an effective spatial resolution of 10x$10\ mm^2$ for the velocity field. The gas concentration was measured in the facility by mean of two mass spectrometers (MS's). Gas was continuously sampled through capillaries and sent to the MS systems through small tubes. The MS measurement is sequential and only one line can be selected at a time via a multiport rotating valve per mass spectrometer. When selected, the sampled gas is sent to a quadrupole mass spectrometer which gives the partial pressure of the selected gas (air or helium). From these partial pressures, the concentrations and the densities were calculated. The MS capillaries as well as the thermocouples which were not used for the present experiments are mounted on instrumentation wires throughout the entire vessel. Three horizontal and one small vertical instrumentation wires are visible in the PIV recording in Figure 2 a). The density stratification derived from a MS measurement for experiment EOLIE_20 in the axis of symmetry of the vessel for $t = 0\ s$ can be found in Figure 2 b). In the lower part ($y \lesssim 1000\ mm$) the density of the pure air atmosphere amounts to $\rho_{0,air} = 1.187\ kg/m^3$ while the initial density of the helium rich layer ($y \gtrsim 2500\ mm$) is $\rho_{0,l} = 0.776\ kg/m^3$. In between we find a transitional zone with a gradient caused by combined effects of the helium layer build up process and molecular diffusion processes.

Parameters for the experimental series were (i) the jet exit velocity v_0 and (ii) the stratification strength of the Helium rich air layer. The initial jet Reynolds number Re_0 at the tube exit,

$$\mathrm{Re}_0 = \frac{\mathrm{v}_0 \cdot d_t}{\nu_{0,air}} \tag{1}$$

was calculated using the tube inner diameter d_t and the nominal velocity v_0, i.e. we neglect developing boundary layers at the inner tube walls and assume a perfect top-hat velocity profile at the tube exit. Since the flow rate is kept constant during the entire experiment, this Reynolds number characterizes the momentum flux of the jet injected. To characterize the initial stratification strength we define a densimetric Froude number (Fr) and a mean density difference $\Delta\rho$. The Froude number is calculated as:

$$Fr_0 = \frac{\mathrm{v}_0}{\sqrt{g' \cdot h}} \tag{2}$$

with the reduced gravity:

$$g' = g\frac{\rho_{0,air} - \rho_{0,l}}{\rho_{0,air}} \tag{3}$$

and with a characteristic initial length scale h. For the length scale we chose the vertical distance of the transitional zone $h = 1.5\ m$, Figure 2 b). It is noted that neither the velocity v_0 at the tube exit and nor the chosen length scale do precisely characterize the physics in the mixing zone. Both v_0 and h are probably too high. The centre line axial velocity decays with downstream distance and it might be more appropriate to chose the velocity of a corresponding free jet (having the same exit velocity) at a distance of $y = 1000\ mm$ as the characteristic velocity. Also the penetration depth h_p as depicted in Figure 2 a) based on visual reasoning might be a better choice, but one is faced with the problem of a rigorous definition which can be unambiguously reproduced. This topic is subject of ongoing discussions.

The density difference $\Delta\rho$ depicts the validity or non-validity of the Boussinesq approximation and was calculated as:

$$\Delta\rho = \frac{g'}{g} \cdot 100\ [\%] \tag{4}$$

It should be noted that numerical simulations based on Reynolds Averaged Navier-Stokes (RANS) approaches can yield acceptable accuracy only if the Boussinesq approximation is valid, i.e. the density variation in the continuity equation is neglected and that the density variation generates only a small correction to the inertia term of the momentum equation. The experiments were intentionally designed to violate the Boussinesq approximation, i.e. $\Delta\rho > 10\ \%$. It is, therefore, expected that these experiments with steep density gradients pose some computational challenges.

The experimental parameters of the entire experimental series can be found in Table 1. For the calculations the following physical properties calculated according to [4] were used: Air at a nominal temperature of $T_0 = 20\ ^\circ C$ has a density of $\rho_{0,air} = 1.187\ kg/m^3$ and a kinematic viscosity $\nu_{0,air} = 1.535{\cdot}10^{-5}$ m^2/s^2.

The discussion will focus on the pure air jet experiment E_18 and one jet-layer experiment E_20. The discussion of the other experiments is subject of additional publications. In the next section we start

comparing the turbulence characteristics of the pure air jet with the literature. This is followed by comparing the findings for the pure air jet with the jet-layer experiment.

Exp.	Type	$\dot{m}$ g/s	v_0 m/s	Re_0 –	X_{He} %	$\rho_{0,l}$ kg/m^3	Fr_0 –	$\Delta\rho$ %
E_18	pure jet	15	2.86	14′000	0	–	–	
E_21	pure jet	28	5.33	26′000	0	–	–	
E_20	jet & layer	15	2.86	14′000	40	0.776	1.27	34.7
E_22	jet & layer	15	2.86	14′000	25	0.930	1.60	21.7
E_23	jet & layer	28	5.33	26′000	40	0.776	2.36	34.7
E_19	jet & layer	28	5.33	26′000	25	0.930	2.98	21.7
E_24	jet & layer	28	5.33	26′000	25	0.930	2.98	21.7

Table 1: *Main nominal parameters for the different experiments.*

3 Results

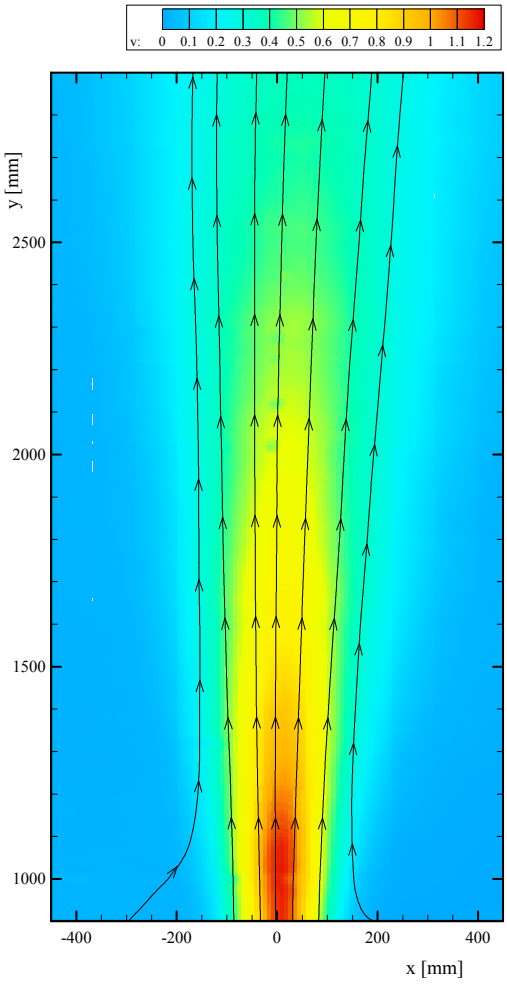

Figure 3: *Downstream development of the axial velocity during the pure air jet experiment* E_18.

Pure air jet experiments. The downstream development of the axial velocity (v) of the pure air jet experiment (E_18) is presented in Figure 3 as a color coded map where stream lines were added. After a linear interpolation of the results to a common grid having a size of 110x220, the three succesively recorded FOV's, Figure 1 a), were 'stitched' together making use of the steady state assumption. The resulting FOV covers a range of $\approx$ 0.9x2.0 m^2. Except for the weak off-axis displacement far downstream ($y > 2000\ mm$) we find a velocity map distribution as expected and described in the literature [7, 6, 5]. The axial velocity profiles can be presented in self similar coordinates. The necessary local characteristic length scale – the half-width radius $r_{0.5}$ – and the local characteristic velocity scale – the maximum velocity $\overline{\mathrm{v}}_{fc}$ – can be derived from applying the Gaussian fit function

$$\overline{\mathrm{v}}(x) = \overline{\mathrm{v}}_{fm} + \overline{\mathrm{v}}_{fc} \cdot \exp\left\{ -\ln(2) \left(\frac{x - x_c}{r_{0.5}} \right)^2 \right\} \tag{5}$$

to the axial velocity profiles. The horizontal displacement of the velocity is depicted by x_c and a possible velocity offset outside the the jet by $\overline{\mathrm{v}}_{fm}$. Since $\overline{\mathrm{v}}_{fm} \approx 0$ this term is not considered further. Here and in the following we denote time averages with an overbar and fluctuating quantities with a prime according to the common velocity decomposition $\mathrm{v}(t) = \overline{\mathrm{v}} + \mathrm{v}'(t)$. The axial velocity profiles can thus be presented in similar-

ity coordinates $\eta = (x - x_c)/r_{0.5}$ and $\overline{\mathrm{v}}(\eta)/\overline{\mathrm{v}}_{fc}$. An example of an axial velocity profile extracted at $y = 1440\ mm$ from Figure 3 with the corresponding Gaussian fit function according to Eq. 5 is shown in Figure 4 a). Next, the axial velocity profiles were extracted for each y coordinate on the common grid 110x220 which results in 220 velocity profiles $y \in [900\ 2900]\ mm$ and Eq. 5 was applied to each of the profiles by a least square method. From the 220 velocity profiles, we present 11 in non-dimensional form in Figure 4 b).

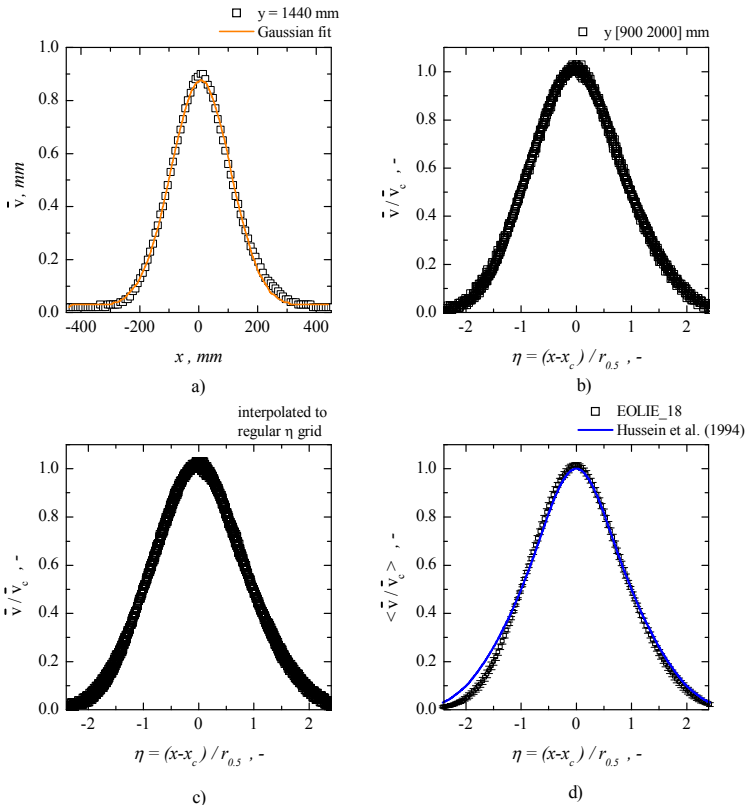

Figure 4: *Normalization and spatially averaging process of the non-dimensional axial velocity profiles for experiment E_18. Mean velocity profile* $\overline{\mathrm{v}(x)}$ *with Gaussian fit at* $y = 1400\ mm$ *a), non-dimensional presentation of* 11 *downstream velocity profiles b), the same profiles as in b) but with an interpolation to a regular grid for* η *c) and spatially averaged non-diemsnional axial velocity profile with error margins and comparison with the literature d).*

To calculate a final representative non-dimensional velocity profile, the individual profiles were linearly interpolated to a regular non-dimensional η coordinate grid, Figure 4 c), and finally all of the 220 profiles were spatially averaged, Figure 4 d),

$$\langle \overline{\mathrm{v}}(\eta) \rangle = \frac{1}{N_\mathrm{v}(\eta)} \sum_i \overline{\mathrm{v}}_i(\eta) \qquad (6)$$

with $N_\mathrm{v}(\eta) = 220$ for velocities close to the tube axis and accordingly smaller further away from the axis. Here and subsequently we denote spatial averages with the notation $\langle ... \rangle$. From the the standard deviation of the averaging:

$$\langle \overline{\mathrm{v}}(\eta) \rangle_{RMS} = \sqrt{\frac{1}{N_\mathrm{v}-1} \sum_i \{\langle \overline{\mathrm{v}}(\eta) \rangle - \overline{\mathrm{v}}_i(\eta)\}^2} \qquad (7)$$

we calculated the errors of the mean non-dimensional spatially averaged velocity $\langle \overline{\mathrm{v}}(\eta) \rangle$ according:

$$\varepsilon \langle \overline{\mathrm{v}}(\eta) \rangle = t \cdot \frac{\langle \overline{\mathrm{v}}(\eta) \rangle_{RMS}}{\sqrt{N_e(\eta)}} \qquad (8)$$

where t depicts the 99 % two sided confidence interval taken from the Student's t-distribution for of a system with N_e degrees of freedom. The effective number of samples $N_e(\eta)$ used for the error calculation is by a factor of 10 smaller compared with $N_\mathrm{v}(\eta)$ because adjacent velocity profiles are not statistically independent. Calculating the integral length scale L_v in y direction from the integration of the spatial cross-correlation function of the velocity signal $\mathrm{v}(y)$ reveals that approximately every 22^{nd} velocity profile on the chosen grid (110x220) which corresponds to $\Delta y \approx 100\ mm$ is statistically independent. The results of the corresponding calculations are not presented here. The calculated errors $\varepsilon \langle \overline{\mathrm{v}}(\eta) \rangle$ are depicted in Figure 4 d) by error bars. Comparing our experimental results with previous measurements [2, 7], we find an excellent agreement for the right half of the profile ($\eta > 0$) while on the left side there is some lack of coincidence for $\eta < -1$ which is caused by the weak horizontal deflection of the jet for large downstream distances discussed below.

To further characterize the evolving jet, the development of the parameters $\overline{\mathrm{v}}_{fc}$, $r_{0.5}$ and x_c as derived from the application of Eq. 5 to the axial velocity profiles are presented in Figure 5 for normalized downstream distances $10 < y/d_0 < 40$. Only every 4^{th} measurement point is displayed. The downstream development of the normalized maximum axial velocities as obtained from the Gaussian fit $\mathrm{v}_0/\mathrm{v}_{fc}$ is

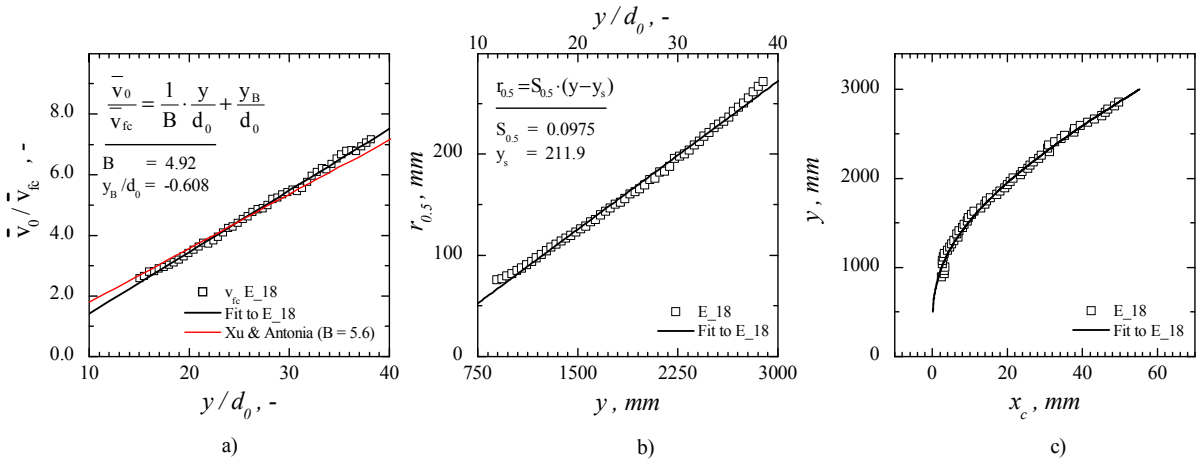

Figure 5: Downstream distance d*evelopment of the parameters* $\overline{\mathrm{v}}_{fc}$, $r_{0.5}$ *and* x_c *derived from the application of Eq.* 5 *to approximate the axial velocity profiles.*

compared in Figure 5 a) with the velocity decay discussed in [8]. For a self similar round jet it is expected that the velocity decays with [2]

$$\frac{\mathrm{v}_0}{\mathrm{v}_{fc}} = \frac{1}{B}\frac{y}{d_0} + \frac{y_B}{d_0} \tag{9}$$

where $y_B = -0.045\ m$ depicts the virtual origin of the jet and $B = 4.92$ is the decay constant when we apply Eq. 9 to the entire range $10 < y/d_0 < 40$. Although there is some scatter for the decay constant B discussed in the literature [5] ($B \in [5.5\ 6.5]$), our value falls below the lower end, indicating that the jet decays on average a bit faster than one would expect it for a free jet. The scatter might be due to the initial jet conditions – a smooth contraction nozzle jet corresponds to $B = 5.6$ and a long pipe jet corresponds to $B = 6.5$ as discussed in [8] – but our low value would suggest having used a contraction nozzle – which was not the case. Excluding data with downstream distances $y/d_0 > 30$ before applying Eq. 9 based on the argument that the jet starts to 'see' the vessel dome and consequently decays faster, results in $B = 5.05$ and $y_B = -0.038\ m$ which improves the result slightly, but does not shift B into the range given in the literature.

The half width radius $r_{0.5}$ used to normalize the radial distance x as a function of downstream distance is presented in Figure 5 b). It is expected that $r_{0.5}$ grows linearly with downstream distance. The growth of $r_{0.5}$ is thus expressed by

$$r_{0.5} = S_{0.5}(y - y_S) \tag{10}$$

where the slope $S_{0.5} = 0.0975$ is the jet's half width spreading rate and $y_S = 211.9\ mm$ is the coordinate of the spreading virtual origin when applying Eq. 10 to the entire range $10 < y/d_0 < 40$.

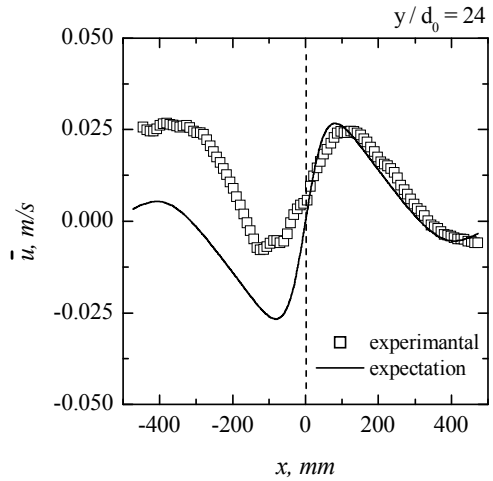

Figure 6: *Horizontal velocity profile* u *at downstream distance* $y/d_0 = 24$.

In contrast to the decay constant B discussed above, we find a reasonable agreement between our value and the literature [5] ($S_{0.5} \in [0.086\ 0.096]$. It is noted that a faster velocity decay as stated above for our experiment can only be achieved by an enhanced entrainment of fluid from regions not affected by the direct influence of the jet ($|\eta| > 2.6$, see Figure 4 d), thus it is expected, that the width of the axial velocity profiles expressed as $r_{0.5}$ must also grow somewhat faster – according to our observations. Finally, we present the horizontal displacement x_c depicting the location of the axial velocity maximum v_{fc} in Figure 5 c). We find a weak but noticeable horizontal displacement x_c which increases with downstream distance having a maximum of $x_c \approx 50\ mm$ at the end of the range $10 < y/d_0 < 40$ considered here. This deflection is probably caused by the non-point symmetry of the horizontal velocity profile $\overline{u}$ across the jet, Figure 6. As expected, $\overline{u}$ decays for $x > 400\ mm$ to

almost zero, but for $x < -300\ mm$ we find a persistent velocity of $\overline{u} \approx 2.5\ cm/s$ projecting towards the jet axis instead of the expected decay to zero. We find similar non-point symmetric horizontal velocity profile shapes for any downstream distance. This weak horizontal velocity projecting towards the jet axis most probably causes the jet deflection (Figure 5 c) as well as the asymmetry of the non-dimensional axial velocity profile (Figure 4 d) by hindering the jet expansion into the outer mixing zone ($\eta < -1$) or even by compressing this zone.

Air jet impinging onto a helium rich air layer. For the helium rich air layer build-up we injected helium for a certain amount of time determined in scoping tests through a tube close to the vessel dome until the desired helium concentration is reached. The initial density profile for experiment E_20 (see also Table 1) measured at the symmetry axis of the test section is shown in Figure 2 b). In the lower part of the vessel we have initially an air atmosphere at room temperature ($T_0 \approx 20\ ^\circ C$) while the helium-air mixture with a lower density is trapped in the vessel dome. For details on the helium filling procedure see [3]. The measurement is initiated by opening a valve to release the air jet ($t = 0\ s$) and the entire experiment is finished when the helium rich layer is completely eroded such that we measure similar densities in the entire vessel ($t \simeq 19'000\ s$). Typical mean axial velocity $\overline{\mathrm{v}}$ and turbulent kinetic energy k maps measured in the air jet impinging onto the helium rich air layer from below are shown in Figure 7 right after the beginning of the jet injection $t_1 = [53\ 463]\ s$ and after the erosion process has proceeded some time $t_2 = [4590\ 5000]\ s$. Consequently, it was necessary to move the FOV from PosA to PosB to follow the erosion process (Figure 1 a). The kinetic energy was calculated by

$$k = \frac{1}{2}\left\{\overline{(\mathrm{v}')^2} + 2 \cdot \overline{(u')^2}\right\} \tag{11}$$

with $\overline{(\mathrm{v}')^2}$ and $\overline{(u')^2}$ depicting the variance of the velocity fluctuations in y and x direction, respectively. Due to its momentum, the jet continuously penetrates upwards into the helium rich layer. Through

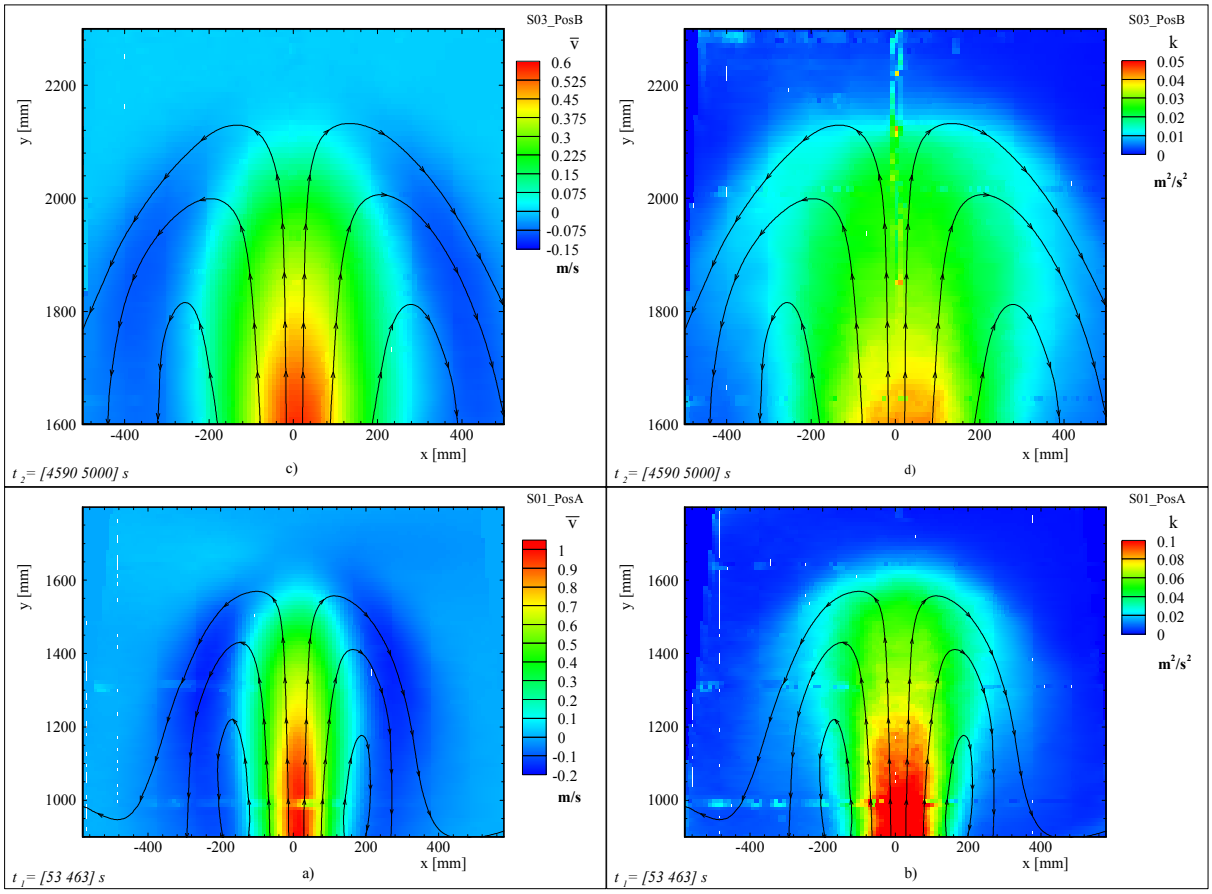

Figure 7: *Mean axial velocity $\overline{\mathrm{v}}$ (a and c) and turbulent kinetic energy k maps (b and d) measured in the air jet impinging onto the helium rich air layer for $t_1 = [53\ 463]\ s$ and $t_2 = [4590\ 5000]\ s$ which corresponds to position A and B in Figure 1 a).*

the action of the negative buoyancy, the axial velocity experiences a strong deceleration in the vicinity of the helium rich layer (the mixing zone), Figure 7 a) and c) and the jet is finally stopped within a distance of $\approx 500\ mm$. Fluid accumulates in a continuous process in this mixing zone and part of the fluid consisting now in an air helium mixture is flowing back in an annular region around the upward flowing jet as indicated by the streamlines. Consequently, the jet decelerates additionally, because the downwards annular flow slows down the upward jet flow. At least for the initial stage of the erosion process, Figure 7 a), the outwards spreading streamlines seems to indicate that the outward flow is not passing all the way down to the jet orifice and eventually even further down to the vessel bottom, but down to a level where the density of the annular flow equals the density of the helium stratification such that the fluid starts to spread radially. The main difference between the early stage of the erosion process (t_1) and a later time (t_2), is the stronger confinement of the flow around the jet for t_1, Figure 7 a) versus c), which can directly be attributed to the spreading through entrainment of ambient fluid of the (free) jet with downstream distance, Figure 5 b). The latter observation equally applies to the turbulent kinetic energy map Figure 7 b) versus d). While we initially find $k \approx 0.1\ m^2/s^2$ in the jet core (t_1), the kinetic energy is later distributed to a larger area such that we find $k \approx 0.04\ m^2/s^2$ (t_2). This finding is detailed in the next figure. The axial velocity and the kinetic energy decay in the jet impingement zone are compared in Figure 8 by means of vertical line profiles extracted at $x = 0\ mm$ with the corresponding values from the free jet experiment (E_18) together with corresponding density profiles for $t_1 = [53\ 463]\ s$ and $t_2 = [4590\ 5000]\ s$. Due to the higher momentum of the jet at t_1, we find the axial velocity $\overline{\mathrm{v}}$ decays to $\overline{\mathrm{v}} \approx 0\ m/s$ beyond the level $y \approx 1400\ mm$, where the density starts decreasing and accordingly, the turbulent kinetic energy approaches $k \approx 0\ m^2/s^2$ also beyond this level, Figure 8 a, b and c. It is also shown that $\overline{\mathrm{v}}$ decays much faster below and in the jet impingement zone compared with a corresponding free air jet while k remains on the same level as for the free jet until it levels off. Later in time (t_2), the decay of $\overline{\mathrm{v}}$ to zero coincides almost with the beginning of the helium stratification, i.e. where ρ decreases, as does the decay of k.

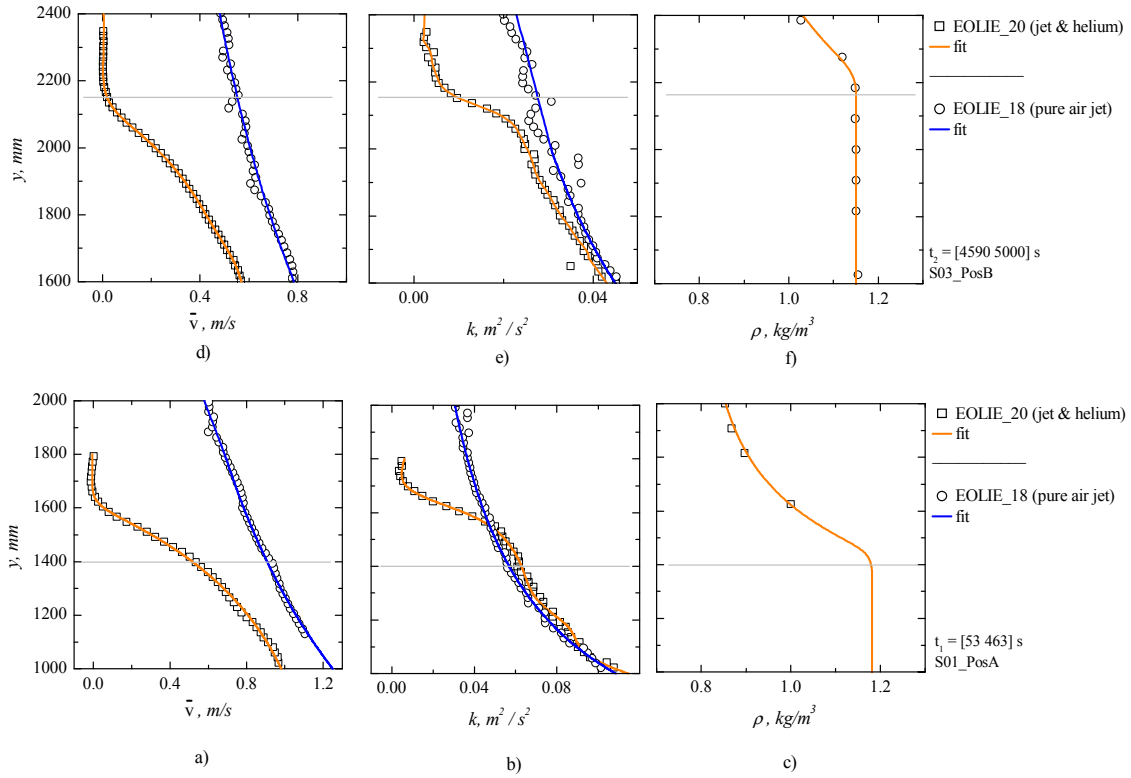

Figure 8: *Vertical line profiles of the mean axial velocity decay* $\overline{\mathrm{v}}$ *(a and d), turbulent kinetic energy* k *decay (b and d) and density profiles (c and f) measured in the mixing zone for* $t = [53\ 463]\ s$ *and* $t = [4590\ 5000]\ s$. *The results for* $\overline{\mathrm{v}}$ *and* k *are compared with corresponding measurements for the free air jet (*E_18).

4 Conclusions and Outlook

A series of fundamental mixing experiments was presented, highlighting the interaction of a vertical air jet emerging from a tube below a helium rich air layer. These experiments were performed in one of the vessels in the large scale PANDA facility having a diameter of $4\ m$ and a height of $8\ m$ located at the Paul Scherrer Institute in Switzerland. Although the vertical jet discharges initially into an neutral environment, the physical characteristics differ from a classical non-buoyant jet. It was shown that the velocity decays faster already below the helium rich layer compared with the non-buoyant jet. After a certain distance, the ambient density continuously decreases such that the non-buoyant jet becomes increasingly negatively buoyant when penetrating the helium rich layer and the axial velocity decays very rapidly. Fluid accumulates in this mixing zone and a part of the fluid is flowing back in a small annulus around the upward flow. By this transient mechanism, the helium layer is continuously eroded and helium is transported into lower parts of the test section such that the jet becomes increasingly negatively buoyant right from the beginning. For comparison purposes, additional experiments were performed for a pure, non-buoyant air jet emerging into the vessel in the absence of the helium stratification but, having the same exit velocity as the stratified case.

From the non-dimensional presentation of the axial velocity $\overline{\mathrm{v}}$ an excellent agreement of the right half of the profile was found when compared with the literature, while the left side shows some lack of coincidence. This was most probably caused by a non-point symmetric profile of the horizontal velocity $\overline{u}$ with a small non-vanishing horizontal velocity component outside the jet which causes a maximum jet deflection of $x_c \approx 50\ mm$ as well as the asymmetry of the non-dimensional axial velocity profile by hindering the jet expansion into the outer mixing zone. The calculated maximum axial velocity decay of the pure jet was faster than corresponding values in the literature and the jet spreading rate defined by the half width radius $r_{0.5}$ at the upper bound of other experiments.

Due to the higher momentum it was found that the jet penetrates initially much deeper into the helium rich stratification compared with later instances in time. Initially, the axial velocity $\overline{\mathrm{v}}$ decays to $\overline{\mathrm{v}} \approx 0\ m/s$ beyond the level where the density starts decreasing and accordingly, the turbulent kinetic energy approaches $k \approx 0\ m^2/s^2$ also beyond this level. It was also shown that $\overline{\mathrm{v}}$ decays much faster below and in the jet impingement zone compared with a corresponding free air jet while k remains on the same level as for the free jet until it levels off. Later in time, the decay of $\overline{\mathrm{v}}$ to zero coincides almost with the beginning of the helium stratification, i.e. where ρ decreases, as does the decay of k.

The other experiments will be analyzed in a similar manner and the ultimate goal is a non-dimensional presentation of the erosion speed as a function of jet momentum and stratification strength.

References

[1] C.-J. Chen and W. Rodi. Vertical turbulent buoyant jets: A review of experimental data. *NASA STI/Recon Technical Report A*, 80:23073–+, 1980.

[2] H. J. Hussein, S. P. Capp, and W. K. George. Velocity measurements in a high-reynolds-number, momentum-conserving, axisymmetric, turbulent jet. *Journal of Fluid Mechanics*, 258:31–75, 1994.

[3] R. Kapulla, D. Paladino, G. Mignot, R. Zboray, and S. Gupta. Break-up of gas stratification in LWR containment induced by negatively buoyant jets and plumes. In *17th International Conference on Nuclear Engineering*, volume 2009, pages 657–666. ASME, 2009.

[4] E. Lemmon, M. Huber, and M. McLinden. *NIST Standard Reference Database 23: Reference Fluid Thermodynamic and Transport Properties-REFPROP, Version 9.0*. National Institute of Standards and Technology, Standard Reference Data Program, 2010.

[5] G. Lipari and P. Stansby. Review of experimental data on incompressible turbulent round jets. *Applied Scientific Research*, 87(1):79–114, 2011.

[6] E. List. Turbulent jets and plumes. *Annual Review of Fluid Mechanics*, 14:189–212, 1982.

[7] S. B. Pope. *Turbulent flows*. Cambridge University Press, 2000.

[8] Xu and Antonia. Effect of different initial conditions on a turbulent round free jet. *Experiments in Fluids*, 33:677–683, 2002. 10.1007/s00348-002-0523-7.